Peak, B.A., et al., 2021, Zircon (U-Th)/He thermochronology reveals pre-Great Unconformity paleotopography in the Grand Canyon region, USA: Geology, v. 49, https://doi.org/10.1130/G49116.1

# Zircon (U-Th)/He thermochronology reveals pre-Great Unconformity paleotopography in the Grand Canyon region

B.A. Peak[1], R.M. Flowers[1], F.A. Macdonald[2], J.M. Cottle[2]

[1]Dept. of Geological Sciences, University of Colorado, Boulder, CO 80309

[2]Earth Science Dept., University of California, Santa Barbara, CA 93106

## Supplementary Text

## FACTORS AFFECTING ZHe DATES

In addition to the influence of radiation damage on ZHe dates as described in the main text, several other factors can also affect ZHe dates: α-ejection, He implantation, parent-nuclide zonation, grain size, and inclusions.

Alpha-ejection is the loss of He atoms from the crystal lattice due to the energy associated with radioactive decay (rather than gas diffusion) (Farley et al., 1996; Ketcham et al., 2011). This effect occurs at grain surfaces and can bias the measured date to be younger than reality. Knowing the geometry and size of the grain, this effect can be corrected for. The magnitude of the α-ejection correction increases for smaller grains.

He implantation occurs when He ejected from one crystal via α-ejection penetrates the crystal lattice of a neighboring grain. In this case, the impacted grain will display dates older than reality due to the extra He (e.g. Murray et al., 2014). This effect is largest in grains with low He concentrations but matters less when high He and U concentrations are present.

Zonation of parent nuclides, or eU-zonation, (hereafter "zonation") within the zircon crystal has the potential to cause dispersion in ZHe date-eU correlations. This is due to three effects of zonation: 1) modification of the α-ejection correction that typically assumes a homogeneous distribution of parent nuclides, 2) deviation of bulk He diffusion between zoned and unzoned grains with the same bulk eU due to spatial variation in intracrystalline radiation damage, and 3) changes in the evolution of the He diffusion profile along a radial transect of the grain (Hourigan et al., 2005; Farley et al., 2011; Johnstone et al., 2013; Orme et al., 2015; Danišík et al., 2017).

Zircon with cores enriched in parent nuclides will generally yield dates older than their unzoned counterparts (Orme et al., 2015), while those with rims enriched in parent nuclides will instead generally yield younger dates than unzoned grains. Intrasample grain variability in zonation pattern is the primary factor in zonation-caused date-eU dispersion (e.g., Ault and Flowers, 2013). A sample with consistent zoning patterns between grains may exhibit dates that differ from unzoned grains with the same bulk eU, but the dates will differ in a consistent way that is not expected to introduce substantial dispersion into the overall date-eU pattern. The effects of zonation are amplified by small grain size.

Larger mineral grains are more He retentive than smaller grains at the same temperature and with an equal degree of radiation damage (Reiners and Farley, 2001). In natural samples, sizes of individual grains can be variable. The effect of grain size must be taken into consideration when interpreting (U-Th)/He data, especially in combination with other grain characteristics such as zonation.

Zircon grains may contain inclusions in the form of enclosed mineral grains—"mineral inclusions," or pockets of enclosed fluids—"fluid inclusions." Avoiding grains with inclusions is preferable because of the possibility that the inclusions contain abundant U, Th, Sm or He, which affects the $\alpha$-ejection correction (that generally assumes uniform parent isotope zonation) and may skew the bulk date calculated for the grain if inclusions are incompletely dissolved. For zircon, the HF dissolution process dissolves all inclusions (unlike for apatite, where the $HNO_3$ dissolution process leaves any zircon inclusions that might be present intact). Fluid inclusions have been

shown to correlate with substantial date-eU dispersion in at least one study (Danišík et al., 2017) and ideally should be avoided due to the unquantified nature of this dispersion.

## SAMPLES

Samples UG90-2 and UG96-1 were collected by S. Bowring. AHe data were published for UG90-2 in Flowers & Farley (2012). Samples CP06-52, CP06-65, CP06-69, CP06-70 and CP06-72 were collected by Flowers. AHe data for these samples were published in Flowers et al. (2008) and Flowers and Farley (2012). EGC1 was collected by Macdonald and U-Pb geochronologic data were published in Rooney et al. (2017). For EGC1, only zircon crystals dated previously by U-Pb LA-ICPMS and shown to be of magmatic (rather than inherited) origin owing to consistency of the U-Pb dates with the unit's 729 ± 0.9 Ma age were analyzed for ZHe. This is the first study to publish ZHe thermochronologic data for any of these samples. Sample locations and relative elevation relationships are shown in Fig. 1A-B, D and given as decimal coordinates when available in Table S1. Locations for samples UG90-2 and UG96-1 were recorded only in river miles and locations shown in Fig. 1 are approximate.

## ANALYTICAL METHODS

### (U-Th)/He Methods

All ZHe data were collected at the University of Colorado Thermochronology Research and Instrumentation Laboratory (CU TRaIL). Individual zircon grains from each sample were picked based on color, size, and euhedral shape using a Leica M614 binocular microscope. Less opaque, and presumably less-damaged, zircon were preferentially targeted for analysis in an effort to select the most He retentive grains most likely to record the Proterozoic history. A representative range of grain sizes, including the largest crystals, were chosen for analysis. All analyzed grains were

whole crystals, except those from Chuar Tuff sample EGC1, in which only zircon fragments were available. Following an initial suite of analyses, we became aware that fluid-inclusion bearing grains yielded dates representing outliers from the larger data patterns, consistent with observations in Danisik et al. (2017). We therefore rejected these grains from our dataset (N = 6 analyses) and avoided all such grains for subsequent ZHe analyses.

Grains were measured and described and then packed in individual niobium tubes. He was measured by degassing each zircon in an ASI AlphaChron 774 He extraction and measurement line. Tubes were then spiked with a $^{235}$U-$^{230}$Th-$^{145}$Nd tracer and dissolved in HF and HCl baths in pressure acid-vapor dissolution vessels at temperatures >200°C. Dissolved solutions were then analyzed for U, Th and Sm with an Agilent 7900 quadrupole ICPMS. Uncorrected dates were calculated from U, Th, Sm and He values and corrected for α-ejection and grain geometry assuming an orthorhombic prism geometry and using the equations of Ketcham et al. (2011) (Table S1-2). We suspect that the zircon fragments dated for EGC1 were likely originally crystals of moderate size such that the He-depleted grain edge was not fully removed during mineral separation, so we also report the corrected dates for this sample. eU is calculated following the equation eU = [U] + 0.238[Th] + 0.0012[Sm]. A conservative uncertainty estimate of 15% is applied to eU values to account for the use of a simplified geometry when computing crystal mass, which is used to calculate eU concentration. Individual ZHe date uncertainties are reported at 2s based on the propagated uncertainties of the U, Th, Sm, and He measurements (Table S1-2).

**Depth-Profiling Methods**

To improve ZHe data interpretation and to determine if zonation is a significant contributor to observed ZHe date dispersion in these samples, radial parent nuclide concentration profiles ($^{28}$Si, $^{90}$Zr, $^{147}$Sm, $^{232}$Th and $^{238}$U) were obtained from 7-8 grains per basement sample using laser-ablation ICP-MS at the University of California Santa Barbara. Methods followed those outlined in Kylander-Clark et al. (2013) and McKinney et al. (2015). Instrumentation consists of a Cetac 193 nm ArF Excimer laser and 'HelEx2' ablation cell coupled to an Agilent 7700S Quadrupole ICP-MS. Data reduction, including corrections for baseline, instrumental drift, and down-hole fractionation were carried out using Iolite v. 2.5 (Paton et al., 2010). Background intensities and changes in instrumental bias were interpolated using a smoothed cubic spline function. Statistics for baselines and on peak intensities were calculated using the mean with a 2σ outlier rejection.

Zircon for depth-profiling were selected to have the same range of color and size as those analyzed for ZHe from the same sample. Zircon grains were mounted on clear tape and ablated perpendicular to the c-axis, from the outer surface to 15-30 μm depths in the crystal (depending on grain radius) using a 20 μm-diameter laser spot. Elemental concentrations for U, Th and Sm were normalized to NIST SRM 612 using the values obtained from GeoReM (http://georem.mpch-mainz.gwdg.de/ downloaded February 2020) and using $^{90}$Zr as an internal standard (assuming stoichiometric abundance in zircon). The resulting internal-standard-corrected profiles are given in Figure S2. Reference zircons GJ-1 and 91500 were measured concurrently (values below), demonstrating accuracy to well within 2% of the accepted values.

| | Sm* | ±** | Th* | ± | U* | ± |
|---|---|---|---|---|---|---|
| GJ-1 Measured | 1.48 | 0.1 | 9.49 | 0.4 | 207 | 6 |
| Reference value*** | 1.42 | 0.2 | 9.51 | 1.0 | 227 | 23 |
| | | | | | | |
| 91500 Measured | 0.37 | 0.1 | 28 | 2 | 65 | 3 |
| Reference value | 0.5 | 0.1 | 30 | 3 | 80 | 8 |

*values in ppm

** uncertainties are 2s
*** Reference values taken from http://georem.mpch-mainz.gwdg.de/ downloaded February 2020.

Corrected profiles were normalized to the mean eU of the profile and radii of 1 as in Johnstone et al. (2013) (Fig. S3). Radial position zero corresponds to the edge of the grain, or beginning of the profile, and radial position one corresponds to the center of the grain. This normalization was done to more easily compare inter- and intra-sample variation in zonation pattern and magnitude. Based on this comparison, representative zonation profiles were chosen and applied in thermal history modeling.

## THERMAL HISTORY MODELING APPROACH AND METHODS

### Lower Granite Gorge

#### *Inverse Modeling*

Samples CP06-65, CP06-69 and CP06-70 were grouped together as one dataset for modeling purposes because together they appear to define a single date-eU relationship implying a common thermal history. CP06-72 was excluded from this modeled suite in order to reduce the uncertainty of including zonation profiles from multiple samples and because the date-eU range encompassed by CP06-72 is covered independently by the other three samples. The data from each of the three samples was binned by eU into two simulated grains, for a total of 6 simulated grains representing the full eU range of the dataset (Table S3). Each simulated grain was input into HeFTy as a single

analysis – all relevant element concentrations, radii, and ages were averaged. Binning serves to account for dispersion introduced by various factors not accounted for in the analytical uncertainty reported for individual grain analyses. To be conservative in uncertainty estimates, the uncertainty associated with the average uncorrected date for each simulated grain was taken to be the standard deviation of the bin or 15% of the uncorrected date, whichever was greater. Representative zonation profiles were chosen based on intrasample zonation patterns using the mean normalized zonation profiles in Figure S3 – i.e. patterns considered outliers and not typical of a given sample were not used. Zonation profiles that deviated more from the mean were chosen as "high zonation" profiles and zonation profiles that deviated least from the mean were chosen as "low zonation" profiles. Profiles were also chosen on the basis of size, with profiles for larger grains applied to simulated grains with large radii and the opposite for simulated grains with small radii. Zircon profiles were normalized to the radius and bulk eU of each simulated grain before being input into HeFTy (Fig. 3D, Table S4).

Time-temperature constraints consistent with geologic features and published thermochronologic data through which all tested tT paths were forced to pass were imposed on inverse thermal history models for the NeoExh and SG Hypotheses. Both hypotheses start at 1400 Ma at 400°C consistent with thermobarometric information (Dumond et al., 2007). Constraints on the Phanerozoic tT path are the same in both models and taken from previous theromchronology studies and preserved geologic constraints (details and rationale in Table S5). In addition, exploration boxes were imposed to test the two exhumation hypotheses and to impose physically possible paths for time periods without preserved geologic constraints (Fig. 3A-B, Table S5). The SG Hypothesis model is forced to exhume to the surface by 1255 Ma and is then reburied during the Mesoproterozoic

consistent with burial by the Grand Canyon Supergroup as preserved in the UGG. The NeoExh Hypothesis model is not forced to exhume until beginning 823 ± 26 Ma, representing normal faulting as suggested by K-Ar in the UGG (Elston and McKee, 1982). The K-Ar date is the average of 5 different whole rock analyses on the 1.1 Ga Cardenas basalts that are interpreted to represent a heating and cooling event by ca. 800 Ma disruption to the Ar system. This may record the exhumation associated with faulting that accommodated the <782-729 Ma Chuar Gp. Taking the c. 782 Ma base of the Chuar Gp as the onset of exhumation that led to surface exposure would not change the key outcome of the modeling.

Paths were allowed to variably heat or cool in three segments between each constraint or exploration field and 25000 paths were tested for each modeled hypothesis. The HeFTy default goodness-of-fit (GOF) thresholds for "good" and "acceptable" fitting paths of 0.5 and 0.05, respectively, were adopted for all initial inverse models. The SG hypothesis for the LGG dataset did not produce fits using these default thresholds, so both the SG and NeoExh models were rerun with 0.01 and 0.001 good and acceptable GOF thresholds so that a direct comparison between model results could be made.

The best fit tT paths yielded by the inverse thermal history models for the NeoExh Hypothesis and SG Hypothesis (Table S6) were used to predict the dates for zircon of the same eU, size, and zonation patterns as the input data for comparison with the observed dataset (Fig. 3C-D). Forward model predictions (Table S7) were fit in MATLAB using polynomial curves to better show the overall predicted date-eU trends (Fig. 3C). This comparison illustrates that the best-fit NeoExh path reproduces the data better than the best-fit SG path. To evaluate how grain size variation and

zonation profile heterogeneity affect this outcome, we also predicted the dates for four different endmember combinations of simulated grain radii and zonation profile: 1) Low magnitude of zonation and maximum radius, 2) Low magnitude of zonation and minimum radius, 3) High magnitude of zonation and maximum radius, and 4) High magnitude of zonation and minimum radius. The minimum and maximum radii were determined from the standard deviation of grain radii within each bin. The zonation profiles were selected based on along-profile deviation from the mean profile eU with "high magnitude" corresponding to the greatest deviation and "low magnitude" corresponding to the lowest deviation. (Fig. S3). Results of this modeling are interpreted in the main text.

**Upper Granite Gorge**

In the UGG, the spatial heterogeneity in data patterns suggests variable magnitudes of Neoproterozoic burial across normal faults. We first carried out forward tT models to evaluate if differences in the pre-Cryogenian thermal history can explain the differences in the ZHe dates for the different samples if the Phanerozoic portion of the tT path is held constant, as implied by the broad uniformity in Phanerozoic sedimentary thicknesses across the region. We also performed inverse models to evaluate the viability of post-Supergroup Cryogenian burial. This was motivated by the observation that Chuar sample EGC1 yields ZHe dates younger than its 729 Ma crystallization age despite being stratigraphically higher and younger than the basement samples, again pointing toward different thermal histories in the UGG. We did not model sample UG90-2 because it exhibits dispersion attributed to zonation that is difficult to model accurately with our available data.

***Forward Modeling***

Our forward modeling exercise tested the "Variable Supergroup Burial Hypothesis," in which the younger dates for basement sample UG96-1 and the older dates for basement sample CP06-52 can be explained by localized Proterozoic burial to different depths owing to offsets across faults that generated disparate burial histories (Fig. S4). Forward model predictions were made in HeFTy by inputting specific tT paths that were used to predict dates for zoned zircon grains with the same eU as the analyzed grains for comparison with the observed dates (Table S8; see Table S9 for assumed zonation profiles). We simulated two tT paths that both assume exhumation to the surface at 1255 Ma consistent with Unkar Gp deposition at that time, and assume the same Phanerozoic thermal history. The tT paths differ only in the heating/burial temperatures between 1100 and 600 Ma (Table S10, Fig. S4). The outcomes show that burial to hotter temperatures (200°C) between 1100 and 600 Ma predicts exclusively Phanerozoic dates, which reproduces the younger data pattern of sample UG96-1 (Fig. S4A). In contrast, burial to lower temperatures (125°C) between 1100 and 600 Ma predicts dates as old as 634 Ma, which reproduces the older dates for lower eU zircon from sample CP06-52 (Fig. S4B). Forward models cannot reproduce dates for the higher eU grains from CP06-52, which may be due to shortcomings of the ZRDAAM at its high damage end, as recognized previously (e.g., Powell et al., 2016; Johnson et al., 2017; Ginster et al., 2019). This modeling suggests that the first-order contrast in the ZHe data patterns between UG96-1 and CP06-52 can be accounted for by differences in Proterozoic burial with a tT history that is otherwise identical and consistent with the geologic context. This outcome is in turn compatible with Proterozoic fault-induced differences in localized burial as the cause of these different burial magnitudes.

***Inverse Modeling***

We carried out inverse thermal history models to test the "Chuar Syncline Hypothesis", in which the Chuar syncline was a site of increased local sedimentation and subsequent incision and erosion while the CP06-52 and UG96-1 basement exposures to the west (present coordinates) in the UGG were not. We compared the results of three inverse tT simulations: 1) a Chuar model starting at 729 Ma tuff eruption that allowed a phase of heating up to 100°C before Cambrian deposition, representing up to 3-4 km of Cryogenian-Ediacaran burial and erosion, 2) a CP06-52 model starting at 1400 Ma that allowed the same burial and erosion phase as the Chuar model, and 3) a UG96-1 model that was the same as the CP06-52 model. Complete details of model constraint and exploration boxes are in Table S11. The three samples were modeled separately because of their different date-eU patterns and, in the case of EGC1, its different crystallization age. EGC1 analyses were binned into two simulated grains representing the eU range of the data (Table S8) and modeled using both the uncorrected and corrected dates. Since the dated zircon are fragments of crystals that likely were of moderate size, such that the He-depleted grain edge was likely not fully removed, the true dates are probably somewhere between the corrected and uncorrected values. We therefore simulate both and treat the two sets as endmembers. CP06-52 and UG96-1 analyses were binned into two and four simulated grains, respectively. We found that the highest eU (~ 1466 ppm) zircon analysis from CP06-52, which has a date of 637 ± 31, cannot be fit by the inverse thermal history models using the ZRDAAM, and was therefore excluded from modeling. It is unclear if this is because this outlier grain represents a spurious result due to an unrecognized factor such as a fluid inclusion or extreme zonation, or if this is due to issues with the ZRDAAM at its high damage end (e.g., Powell et al., 2016; Johnson et al., 2017; Ginster et al., 2019).

The Chuar model yields good fit tT paths (using default HeFTy fit criteria of 0.5 for the mean GOF value) that allow Cryogenian heating up to the 100°C upper temperature bound of the simulation whereas the CP06-52 model does not generate good-fit tT results with substantial post-729 Ma Cryogenian heating that fit the input data (Fig. S5A-C). Together this is consistent (but does not alone require) that EGC1 and CP06-52 underwent different thermal histories corresponding to different magnitudes of Cryogenian-Ediacaran burial, compatible with the Chuar Syncline Hypothesis. Inverse modeling for sample UG96-1 (Fig. S5D) was consistent with the results for CP06-52, but produced tT paths with poorer fits than the EGC1 and CP06-52 models. Forward model predictions using the best-fit paths generated by inverse modeling (Fig. S5E) show the degree to which the best-fit paths from each model reproduce the ZHe dates for each sample. The outcomes of this modeling permit the Chuar Syncline hypothesis to be correct, where greater post-Supergroup heating/burial in Cryogenian time affected the Chuar sample than the basement samples outside the Chuar syncline. But such a history is not necessarily required to explain the data.

**REFERENCES CITED**

Danišík, M., McInnes, B.I.A., Kirkland, C.L., McDonald, B.J., Evans, N.J., and Becker, T., 2017, Seeing is believing: Visualization of He distribution in zircon and implications for thermal history reconstruction on single crystals: Science Advances, v. 3, p. 1–10, doi:10.1126/sciadv.1601121.

Dumond, G., Mahan, K.H., Williams, M.L., and Karlstrom, K.E., 2007, Crustal segmentation, composite looping pressure-temperature paths, and magma-enhanced metamorphic field gradients: Upper Granite Gorge, Grand Canyon, USA: Bulletin of the Geological Society of America, v. 119, p. 202–220, doi:10.1130/B25903.1.

Elston, D.P., and McKee, E.H., 1982, Age and correlation of the late Proterozoic Grand Canyon disturbance, northern Arizona.: Geological Society of America Bulletin, v. 93, p. 681–699, doi:10.1130/0016-7606(1982)93<681:AACOTL>2.0.CO;2.

Farley, K.A., Shuster, D.L., and Ketcham, R.A., 2011, U and Th zonation in apatite observed by laser ablation ICPMS, and implications for the (U-Th)/He system: Geochimica et Cosmochimica Acta, v. 75, p. 4515–4530, doi:10.1016/j.gca.2011.05.020.

Farley, K.A., Wolf, R.A., and Silver, L.T., 1996, The effects of long alpha-stopping distances on (U-Th)/He ages: Geochimica et Cosmochimica Acta, v. 60, p. 4223–4229, doi:10.1016/S0016-7037(96)00193-7.

Flowers, R.M., and Farley, K.A., 2012, Apatite 4He/3He and (U-Th)/He Evidence for an Ancient Grand Canyon: Science, v. 338, p. 1616–1620.

Flowers, R.M., Wernicke, B.P., and Farley, K.A., 2008, Unroofing, incision, and uplift history of the southwestern Colorado Plateau from apatite (U-Th)/He thermochronometry: Bulletin of the Geological Society of America, v. 120, p. 571–587, doi:10.1130/B26231.1.

Ginster, U., Reiners, P.W., Nasdala, L., and Chanmuang N., C., 2019, Annealing kinetics of radiation damage in zircon: Geochimica et Cosmochimica Acta, v. 249, p. 225–246, doi:10.1016/j.gca.2019.01.033.

Guenthner, W.R., Reiners, P.W., Ketcham, R.A., Nasdala, L., and Giester, G., 2013, Helium diffusion in natural zircon: radiation damage, anisotropy, and the interpretation of zircon (U-TH)/He thermochronology: American Journal of Science, v. 313, p. 145–198, doi:10.2475/03.2013.01.

Hourigan, J.K., Reiners, P.W., and Brandon, M.T., 2005, U-Th zonation-dependent alpha-ejection in (U-Th)/He chronometry: Geochimica et Cosmochimica Acta, v. 69, p. 3349–

3365, doi:10.1016/j.gca.2005.01.024.

Johnstone, S., Hourigan, J., and Gallagher, C., 2013, LA-ICP-MS depth profile analysis of apatite: Protocol and implications for (U-Th)/He thermochronometry: Geochimica et Cosmochimica Acta, v. 109, p. 143–161, doi:10.1016/j.gca.2013.01.004.

Ketcham, R.A., Gautheron, C., and Tassan-Got, L., 2011, Accounting for long alpha-particle stopping distances in (U-Th-Sm)/He geochronology: Refinement of the baseline case: Geochimica et Cosmochimica Acta, v. 75, p. 7779–7791, doi:10.1016/j.gca.2011.10.011.

Kylander-Clark, A.R.C., Hacker, B.R., and Cottle, J.M., 2013, Laser-ablation split-stream ICP petrochronology: Chemical Geology, v. 345, p. 99–112, doi:10.1016/j.chemgeo.2013.02.019.

McKinney, S.T., Cottle, J.M., and Lederer, G.W., 2015, Evaluating rare earth element (REE) mineralization mechanisms in Proterozoic Gneiss, Music Valley, California: Bulletin of the Geological Society of America, v. 127, p. 1135–1152, doi:10.1130/B31165.1.

Orme, D.A., Reiners, P.W., Hourigan, J.K., and Carrapa, B., 2015, Effects of inherited cores and magmatic overgrowths on zircon (U-Th)/He ages and age-eU trends from Greater Himalayan sequence rocks, Mount Everest region, Tibet: Geochemistry Geophysics Geosystems, v. 16, p. 2499–2507, doi:10.1002/2014GC005684.Key.

Paton, C., Woodhead, J.D., Hellstrom, J.C., Hergt, J.M., Greig, A., and Maas, R., 2010, Improved laser ablation U-Pb zircon geochronology through robust downhole fractionation correction: Geochemistry, Geophysics, Geosystems, v. 11, doi:10.1029/2009GC002618.

Reiners, P.W., and Farley, K.A., 2001, Influence of crystal size on apatite (U-Th)/He thermochronology: An example from the Bighorn Mountains, Wyoming: Earth and Planetary Science Letters, v. 188, p. 413–420, doi:10.1016/S0012-821X(01)00341-7.

# Zircon (U-Th)/He thermochronology reveals pre-Great Unconformity paleotopography in the Grand Canyon region

B.A. Peak[1], R.M. Flowers[1], F.A. Macdonald[2], J.M. Cottle[2]

[1]Dept. of Geological Sciences, University of Colorado, Boulder, CO 80309

[2]Earth Science Dept., University of California, Santa Barbara, CA 93106

## Supplementary Figures

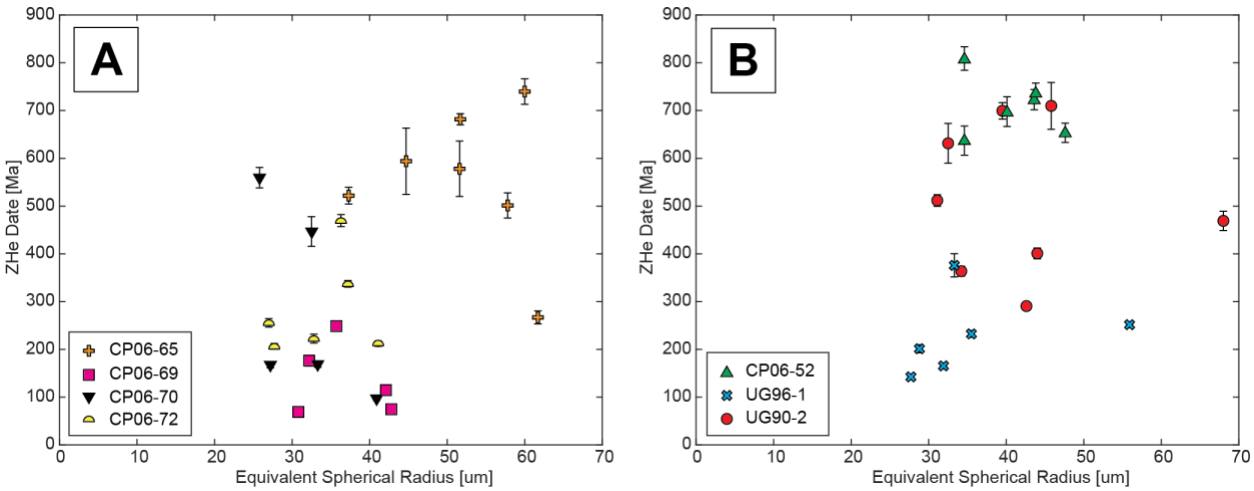


**Figure S1**. ZHe date-equivalent spherical radius plots for **A)** Lower Granite Gorge and **B)** Upper Granite Gorge. Data do not show a strong correlation with radius. EGC1 is not plotted because the grains analyzed were fragments that likely had some of their diffusive profile removed and no correlation with radius is expected. ZHe date uncertainty reported at 2s. Uncertainty is commonly smaller than the data marker symbols.

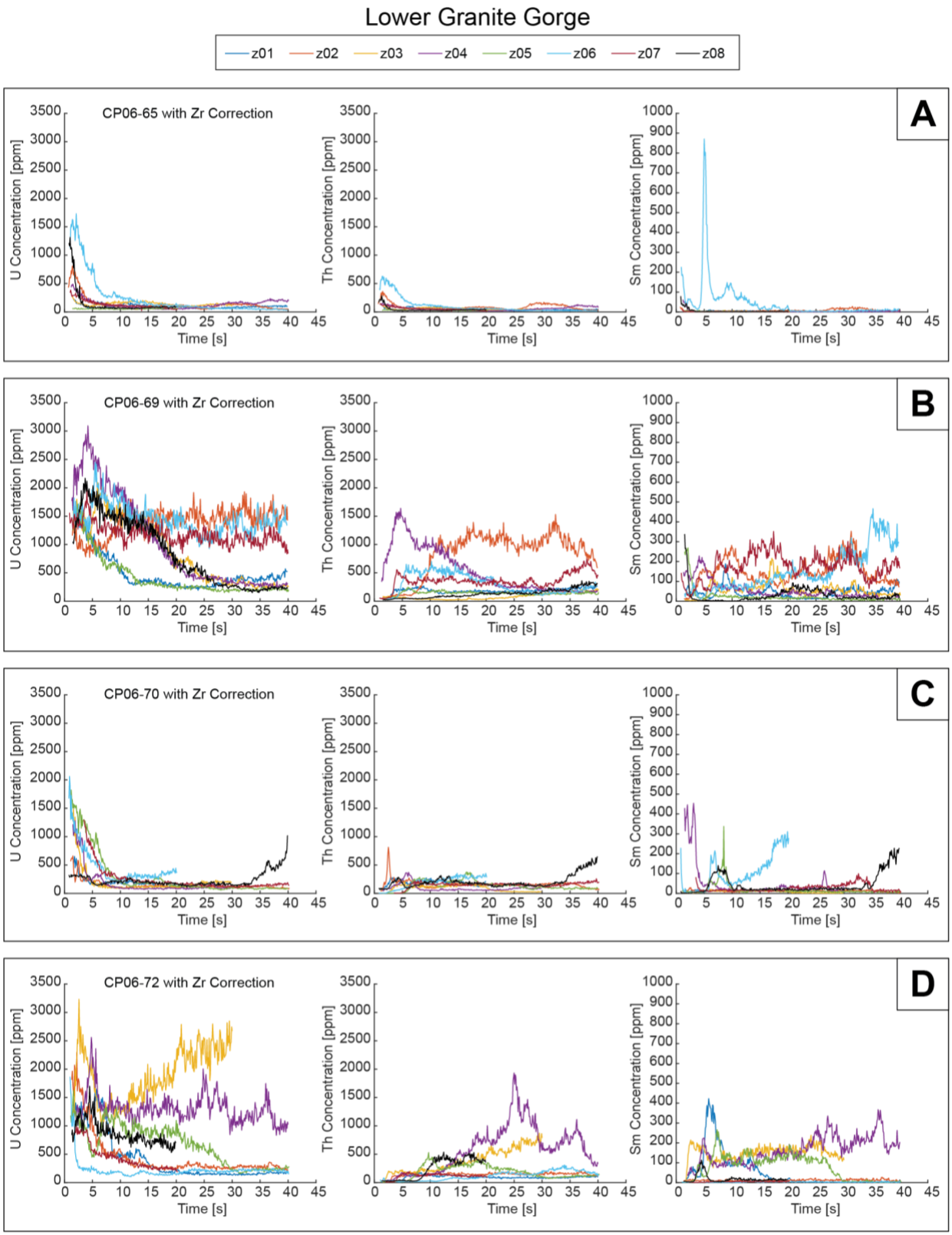
Lower Granite Gorge
z01
z02
z03
z04
z05
z06
z07
z08
A
CP06-65 with Zr Correction
B
CP06-69 with Zr Correction
C
CP06-70 with Zr Correction
D
CP06-72 with Zr Correction
U Concentration [ppm]
Th Concentration [ppm]
Sm Concentration [ppm]
Time [s]

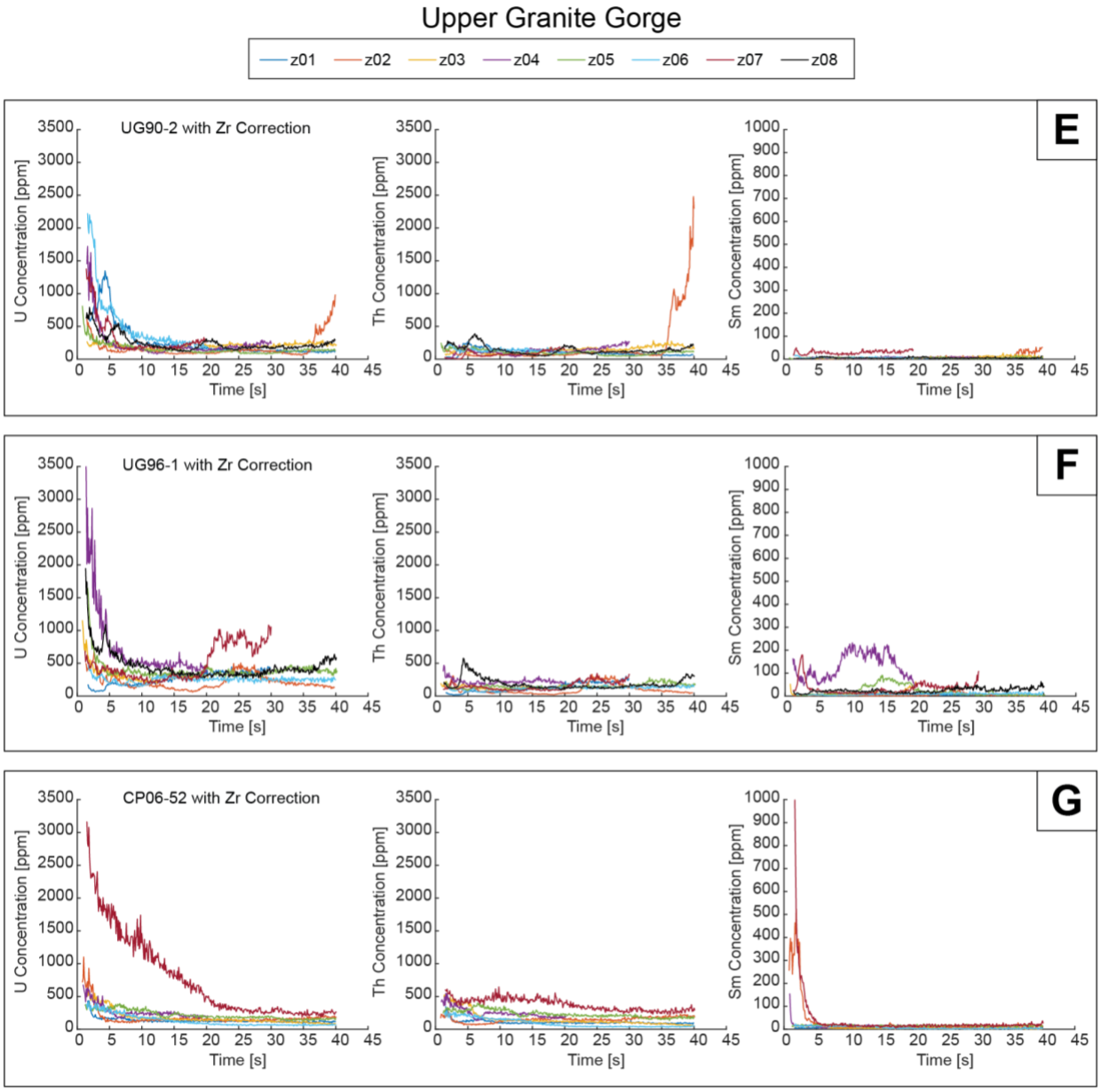


**Figure S2.** Zr-corrected U, Th and Sm concentration profiles for all depth-profiled grains for **A)** CP06-65, **B)** CP06-69, **C)** CP06-70, **D)** CP06-72, **E)** UG90-2, **F)** UG96-1, **G)** CP06-52. Profiles were normalized using Zr as an internal standard to ensure consistency across the entire profile.

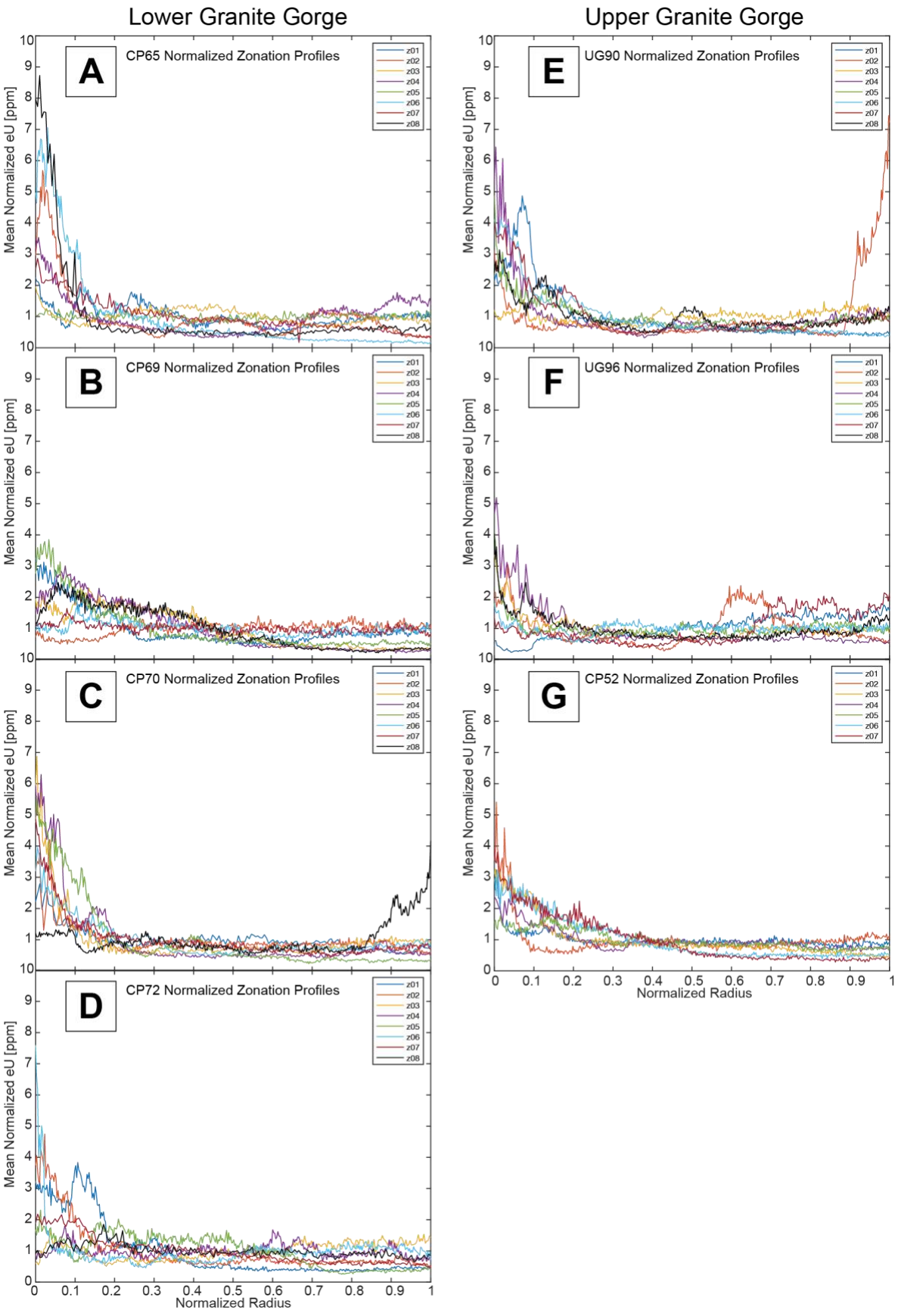
Lower Granite Gorge
Upper Granite Gorge
A
CP65 Normalized Zonation Profiles
B
CP69 Normalized Zonation Profiles
C
CP70 Normalized Zonation Profiles
D
CP72 Normalized Zonation Profiles
E
UG90 Normalized Zonation Profiles
F
UG96 Normalized Zonation Profiles
G
CP52 Normalized Zonation Profiles
z01
z02
z03
z04
z05
z06
z07
z08
Mean Normalized eU [ppm]
Normalized Radius

**Figure S3.** Zonation profiles normalized to a grain radius of 1 and to the mean eU of each profile for **A)** CP06-65, **B)** CP06-69, **C)** CP06-70, **D)** CP06-72, **E)** UG90-2, **F)** UG96-1, **G)** CP06-52. Radial position corresponds to the edge of the grain and radial position 1 corresponds to the center. These normalized profiles were used to assign profiles to each tT modeling bin based on magnitude of zonation (deviation from mean eU, or 1) and grain size (see Fig. S2, relative sizes are indicated by the profile time scale on the x axis). Profiles chosen for modeling purposes are given in Table S4 for the LGG samples and Table S9 for the UGG samples and shown normalized to model bins in Figure 3C.

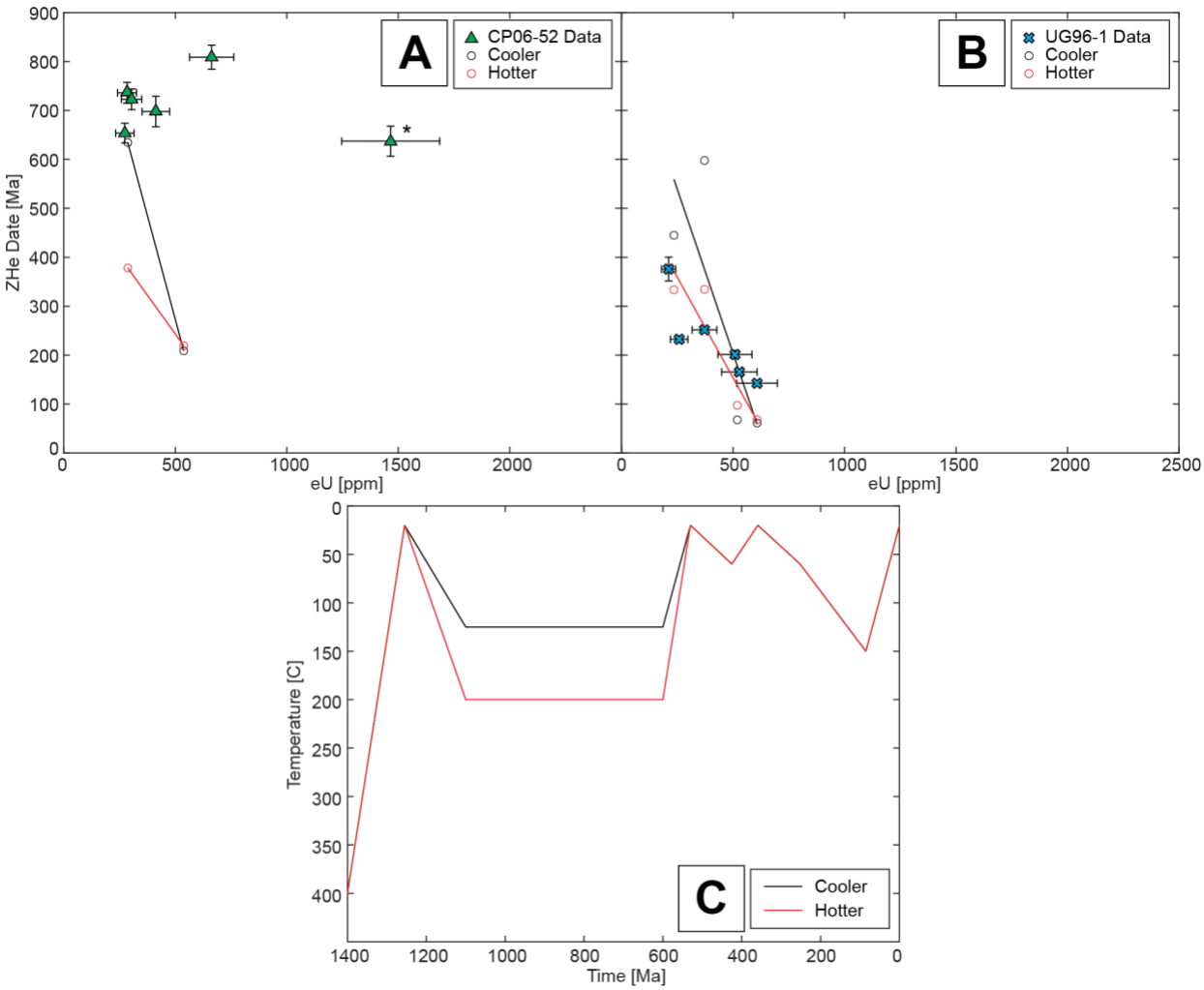


**Figure S4.** Forward model comparisons to evaluate the "Variable Supergroup Burial Hypothesis". ZHe date-eU plots for **A)** CP06-52 and **B)** UG96-1 data, with the dates predicted by the forward models shown in **C)**. * represents CP06-52 analysis excluded from the modeling. **C)** Temperature-time diagram showing the tested forward models. The only segment of the tT paths that vary is between 1100 and 600 Ma. The Cooler path better predicts the CP06-52 dates and the Hotter path better predicts the UG96-1 dates. See supplementary text and Table S10 for additional information.

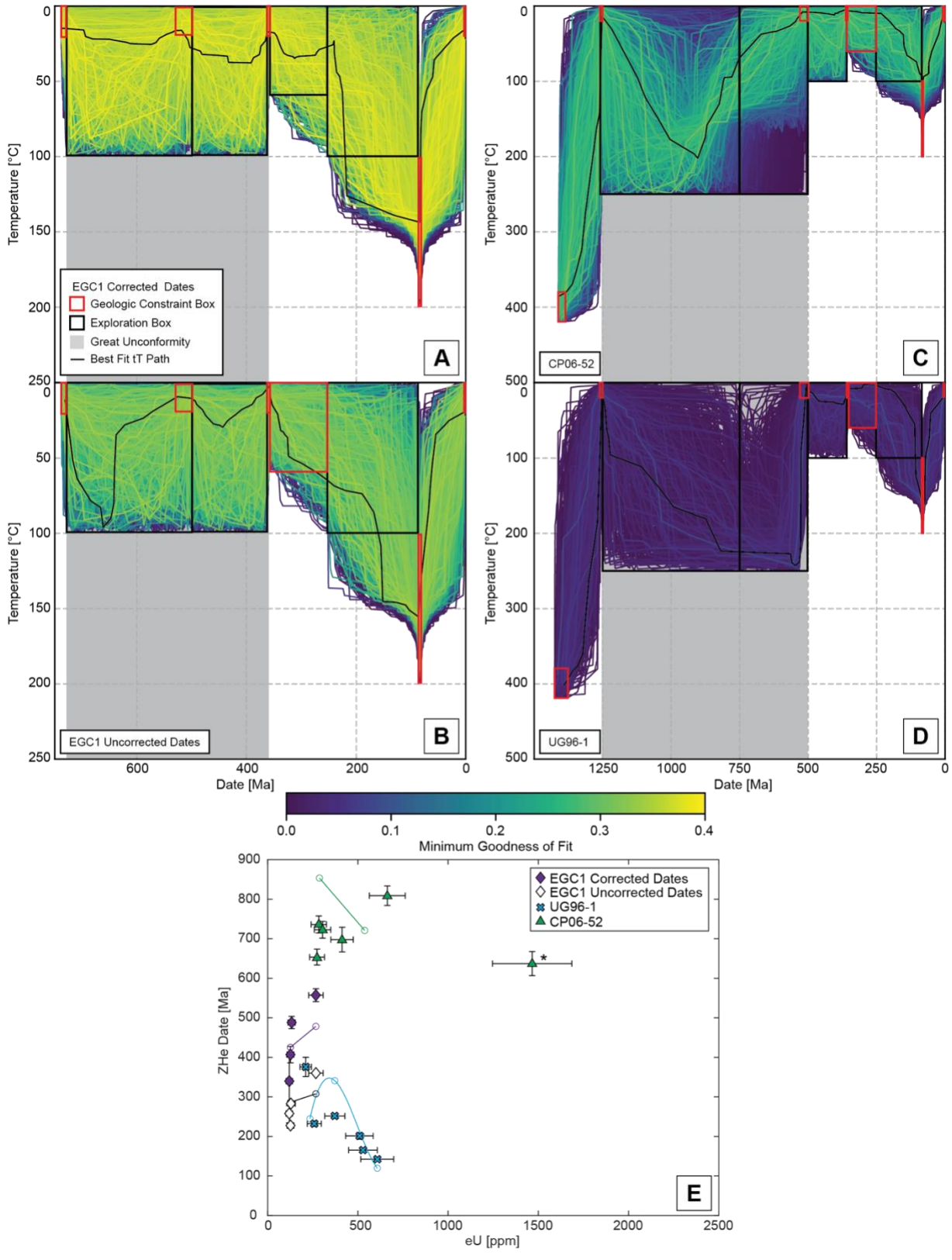
EGC1 Corrected Dates
Geologic Constraint Box
Exploration Box
Great Unconformity
Best Fit tT Path
A
EGC1 Uncorrected Dates
B
CP06-52
C
UG96-1
D
Temperature [°C]
Date [Ma]
Minimum Goodness of Fit
0.0
0.1
0.2
0.3
0.4
EGC1 Corrected Dates
EGC1 Uncorrected Dates
UG96-1
CP06-52
ZHe Date [Ma]
eU [ppm]
E

**Figure S5.** Inverse tT modeling results for the Chuar Syncline Hypothesis for **A)** EGC1 corrected dates, **B)** EGC1 uncorrected dates, **C)** CP06-52, and **D)** UG96-1. Input values for simulated grains are in Table DR3. The EGC1 zircon are fragments of crystals that likely were of moderate size, the true dates are probably somewhere between the corrected and raw values, so we simulate both and treat the two sets as endmembers. The color of each path corresponds to the minimum bin GOF predicted by that path. Bold black line marks the best-fit model tT path prediction. Full descriptions of geologic constraints and exploration boxes used in modeling are in Table S11. **E)** ZHe date-eU plot for EGC1, CP06-52, and UG96 data. * represents CP06-52 analysis excluded from the modeling. ZHe dates predicted by the best-fit tT paths from the inverse models (unfilled circles) are shown for all samples. Predictions are fit with polynomial curves to better show the predicted date-eU trend. Individual simulated grain predictions are in Table S10.